

Code switching revisited: low-overhead magic state preparation using color codes

Lucas Daguerre¹ and Isaac H. Kim²

¹*Department of Physics and Astronomy, University of California, Davis, CA, 95616, USA*

²*Department of Computer Science, University of California, Davis, CA, 95616, USA*

(Dated: October 21, 2024)

We propose a protocol to prepare a high-fidelity magic state on a 2D color code using a 3D color code. Our method modifies the known code switching protocol with (i) a transversal gate between the 2D and the 3D code and (ii) a judicious use of flag-based post-selection. We numerically demonstrate that these modifications lead to a significant improvement in the fidelity of the magic state. For instance, subjected to a uniform circuit-level noise of 10^{-3} , our code switching protocol yields a magic state encoded in the distance-3 2D color code with a logical infidelity of $4.6 \times 10^{-5} \pm 1.6 \times 10^{-5}$ (quantified by an error-corrected logical state tomography) with a 84% of acceptance rate. Used in conjunction with a more recently proposed post-selection approach, extrapolation from a polynomial fit suggests a fidelity improvement to 5.1×10^{-7} for the same code. Finally, we also present a novel simulation technique akin to an extended stabilizer simulator which effectively incorporates the non-Clifford T -gate.

I. INTRODUCTION

An essential step towards building a large-scale fault-tolerant quantum computer is quantum error correction [1]. In principle, the overhead associated with fault-tolerance is merely polylogarithmic in the size of the computation [2], and can be even brought down to a constant [3]. However, the practical overhead needed for large-scale fault-tolerant quantum computation remains daunting.

It has been often stated in the literature that the most costly part of quantum computation is magic state distillation [4]. Traditional methods for magic state distillation relied on multi-level distillation of various protocols [4–15]. Such analysis often led to an enormous overhead in preparing a magic state, motivating novel alternative methods. One of the important recent insights in reducing the overhead is that the size of the codes used at a lower level of distillation need not be as large [16, 17].

Even more recently, there has been a new line of works that aim to prepare a higher-fidelity magic state before the distillation steps. An initial work in this direction is due to Li, who pointed out that the quality of the magic state can be improved by from a judicious post-selection [18]. Chamberland and Noh then used the flag-based methods [19–21] to prepare a magic state while detecting error with a small code [22]. While this work required a relatively challenging physical error rate of 10^{-4} , recent improvements in this direction led to new protocols that can achieve substantial reduction in error even at a realistic physical error rate of 10^{-3} [23–25]. These protocols all boast a rather modest requirement on the number of qubits, which make them attractive quantum error correction protocols to im-

plement and test in the near term; see Ref. [26] for a recent experiment, for instance. These methods, together with recent efficient magic state distillation protocols [17, 27] are expected further reduce the overhead in magic state distillation. In particular, Ref. [25] reported a scheme that can reach an error rate as low as 2×10^{-9} (with the post-selection success probability of 1%) under the same physical error rate. This is a level of error that is sufficient to run some quantum algorithms that have low resource requirement, e.g., [28], obviating the need for magic state distillation entirely for such applications.

However, it should be noted that there are important quantum algorithms requiring a number of T -gates that is still larger than the distillation-free methods can tolerate. For instance, the number of Toffoli gates used in quantum chemistry applications such as FeMoCo ranges between 5.3×10^9 [29] and 1.0×10^{10} [30]. Depending on the specifics of how the Toffoli gate is being used, each Toffoli can be converted to Clifford gates and between 4 and 7 T -gates [31]. Other applications in quantum chemistry tend to require even more T -gates [32–34]. Even with the most recent method, a completely distillation-free approach cannot yet reach an error rate required for these applications. Therefore, an outstanding question is whether it is possible to bring down the cost of T -gate even further, so that its cost is comparable to other Clifford gates in this regime.

This paper introduces a different protocol that aims to achieve a similar goal. Unlike the recent protocols that aim to measure a transversal Clifford gate [24, 25], our approach aims to exploit a code with a non-Clifford transversal gate; such an approach was suggested as an alternative possibility very recently in Ref. [25]. More specifically, we use

the 3D color code [35], and focus on its simplest instance, which is the 15-qubit quantum Reed-Muller code (qRM). We will aim to use the transversal gate of the 3D color code, which is then converted to the 2D color code [36, 37]. While a careful study has suggested that preparation of magic state using 3D color code using this approach is more costly than the multi-level distillation method [38], a more recent work exploited post-selection and flag-qubits [19–21] to improve the performance [23]. Our approach is similar in spirit, though we use the flag qubits in a different way and also uses a novel transversal gate between 3D color code and 2D color code (that is equivalent up to a transversal unitary to the recently discovered gate in Ref. [39], which appeared during the preparation of our manuscript.) Overall, our approach yields a high quality magic state on par with these prior results, which we discuss further in Section II.

Although our protocol has a logical infidelity lower than what was reported in Ref. [24, 25] for similar setups (in terms of the code being used and the physical error rate), they are incomparable. Ref. [24, 25] focused on quantum computing architectures equipped with nearest-neighbor gates on a two-dimensional grid, targeting superconducting qubit-based quantum computers [40]. Our approach uses gates that would require non-local connectivity. As such, our scheme, as it stands, cannot be used directly on these devices.

We emphasize, however, that our protocol is aimed at other types of quantum computers, such as the ones based on photons [41–43], ions [44–46], and neutral atoms [47, 48]. Non-local gates can be accommodated in these architectures, making them promising candidates to implement our protocol.

The rest of this paper is organized as follows. In Section II, we compare our protocol to the other related protocols in the literature. In Section III, we review aspects of color codes. In Section IV, we describe our protocol. In Section V we describe our simulation method and present the result. We end with a discussion in Section VI.

II. COMPARISON WITH PRIOR WORK

A comparison of the infidelity of magic states prepared in our protocol with some recent results in the literature can be found in Table I and II.

A common feature of all these protocols is that they rely on some degree of post-selection. However, there is also a difference in the overall approach. Our protocol (similar to Ref. [23]) uses a transversal non-Clifford gate, whereas Ref. [24, 25, 49] uses the measurement of logical Clifford operators.

Uniform depolarizing noise		
Method	Infidelity	Acceptance rate
Our protocol (error correction)	$4.6 \times 10^{-5} \pm 1.6 \times 10^{-5}$	84%
Butt <i>et al</i> [23]	10^{-4}	94%
Our protocol ^(*) (post-selection)	5.1×10^{-7}	84%
Gidney <i>et al</i> [25]	6×10^{-7}	65%
Itogawa <i>et al</i> [24]	10^{-4}	70%

TABLE I. Infidelity of magic states $|\bar{T}\rangle$ under a uniform depolarizing error model with strength $p = 10^{-3}$, for some state-of-the-art protocols, prepared on the Steane code $[[7, 1, 3]]$. The label “error correction/post-selection” implies that the infidelity of the magic states is quantified via state tomography, where the final state in the post-processing stage is either error corrected or post-selected if syndromes are trivial, respectively. The first two rows use error correction, while the last three rows use post-selection. ^(*)These results are extrapolated from the data points of Fig 8 and 9, following (23) and (24).

Multiparameter depolarizing noise		
Method	Infidelity	Acceptance rate
Our protocol (error correction)	$9 \times 10^{-5} \pm 2 \times 10^{-5}$	71%
Butt <i>et al</i> [23]	$1.6 \times 10^{-4} \pm 2 \times 10^{-5}$	82%
Postler <i>et al</i> [49]	$10^{-4} \pm 3 \times 10^{-5}$	85%

TABLE II. Infidelity of magic states $|\bar{T}\rangle$ ($|\bar{H}\rangle$) states for [49] under a multiparameter depolarizing error model with initialization and measurement error $p_i = p_m = 10^{-3}$, single-qubit error $p_1 = 10^{-3}$, and two-qubit error $p_2 = 3 \times 10^{-3}$, for some state-of-the-art protocols, prepared on the Steane code $[[7, 1, 3]]$. The infidelity of these magic states are quantified via state tomography, where the final state in the post-processing stage is error corrected. The numerical values for the protocol [49] were obtained from Ref. [23].

For our work, an important caveat is that the logical error rate estimate for the magic state was based on an “ungrown” patch of fixed distance $d = 3$. In order to assess the quality of the magic state that will be used in practice, one needs to estimate the fidelity after converting this state to a magic state encoded in a larger-distance code [25]. We instead focus on estimating the fidelity for the $d = 3$ code; the error analysis related to the patch growth is left for future work.

Nonetheless, we can compare our protocols to the

other protocols in the literature that studied the quality of the magic state on an ungrown patch. There are two types of works in the literature, depending on how one quantifies the quality of the magic state. In the first approach, one performs a logical state tomography at the final step, by performing noiseless measurement on all the qubits followed by an error correction. In the second approach, one instead post-selects on observing a trivial syndrome.

In the first approach, our numerical simulation reports a lower infidelity than the results in the literature, using identical error models; see Table I and II. For the second approach, we were unable to directly simulate at a physical error rate used in the literature; the infidelity resulting from the second approach is too low. Instead, we fitted the logical error rate with a polynomial at higher physical error rate and extrapolated. Needless to say, the result obtained this way cannot be directly compared to the results obtained from exact diagonalization [24, 25]. Nonetheless, it can serve as a proxy to understand how well our method would work.

III. COLOR CODES

In this Section, we provide a brief review of the two- and three-dimensional color code [35, 36] that are relevant to this paper. This Section will introduce a convention for the qubit labels we use, which shall be used throughout this paper; see Fig. 1 and 2.

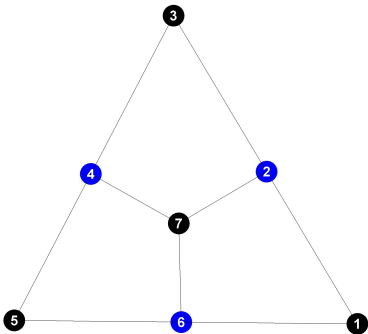


FIG. 1. Pictorial representation of the $[[7, 1, 3]]$ Steane code including labels for the physical qubits.

Most of the results in this Section are well-known, but the discussion about a transversal gate between the two codes is relatively new. A similar transversal gate recently appeared in Ref. [39], which is equivalent to ours up to a transversal unitary.

The two-dimensional color code we consider is a CSS code with parameters $[[7, 1, 3]]$, also known as

the Steane code [50]. The Steane code stabilizer group is generated by mutually commuting Z -type and X -type 2-cells (henceforth referred to as plaquettes) stabilizers, described in Table III.

Steane: $Z(X)$ -type stabilizers			
p_1	$Z_1 Z_2 Z_6 Z_7$	p_4	$X_1 X_2 X_6 X_7$
p_2	$Z_2 Z_3 Z_4 Z_7$	p_5	$X_2 X_3 X_4 X_7$
p_3	$Z_4 Z_5 Z_6 Z_7$	p_6	$X_4 X_5 X_6 X_7$

TABLE III. Z -type and X -type plaquette stabilizer generators for the $[[7, 1, 3]]$ Steane code.

The Steane code encodes a single logical qubit and has minimum weight-3 transversal logical \bar{Z} and \bar{X} operators

$$\bar{Z} = Z_1 Z_2 Z_3, \quad (1)$$

$$\bar{X} = X_1 X_2 X_3. \quad (2)$$

Given that the distance $d = 3$, the Steane code is capable of correcting arbitrary weight-1 errors, and detecting arbitrary weight-2 errors. Unfortunately, the Steane code does not support a transversal logical non-Clifford gate like the T -gate, given that it would violate the no-go Eastin-Knill theorem [51], which states that no stabilizer quantum code exist that contain a transversal universal gate set.

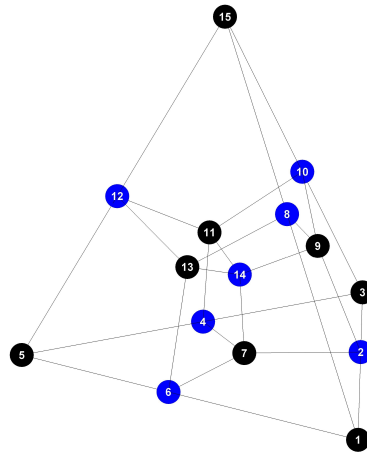


FIG. 2. Pictorial representation of the $[[15, 1, 3]]$ qRM code including labels for the physical qubits.

The three dimensional color code we consider is a CSS code with parameters $[[15, 1, 3]]$. It is the smallest color code in three dimensions that admits a transversal T -gate and represents a specific instance of a family of codes known as quantum Reed-Muller codes (qRM).

The stabilizer group is generated by Z -type 2-cells (plaquettes) and X -type 3-cells. In total there are eighteen plaquettes (Table IV) and four 3-cells (Table V). Since the qRM encodes a single logical qubit and $15 = 1 + 10 + 4$, there are only 10 independent Z -type stabilizers, meaning that there are 8 independent constraints (Table VI). Those are given by multiplying plaquettes around a cylinder, yielding a total of 3 constraints per 3-cell. In a given 3-cell, two such constraints give rise to the third one, thus, two constraints per 3-cell give the net result of 8 independent ones.

qRM: Z -type stabilizers			
p_1	$Z_1 Z_2 Z_6 Z_7$	p_{10}	$Z_6 Z_7 Z_{13} Z_{14}$
p_2	$Z_2 Z_3 Z_4 Z_7$	p_{11}	$Z_2 Z_7 Z_9 Z_{14}$
p_3	$Z_4 Z_5 Z_6 Z_7$	p_{12}	$Z_4 Z_7 Z_{11} Z_{14}$
p_4	$Z_1 Z_6 Z_8 Z_{13}$	p_{13}	$Z_8 Z_{12} Z_{13} Z_{15}$
p_5	$Z_1 Z_2 Z_8 Z_9$	p_{14}	$Z_8 Z_9 Z_{10} Z_{15}$
p_6	$Z_2 Z_3 Z_9 Z_{10}$	p_{15}	$Z_{10} Z_{11} Z_{12} Z_{15}$
p_7	$Z_3 Z_4 Z_{10} Z_{11}$	p_{16}	$Z_8 Z_9 Z_{13} Z_{14}$
p_8	$Z_4 Z_5 Z_{11} Z_{12}$	p_{17}	$Z_9 Z_{10} Z_{11} Z_{14}$
p_9	$Z_5 Z_6 Z_{12} Z_{13}$	p_{18}	$Z_{11} Z_{12} Z_{13} Z_{14}$

TABLE IV. Z -type plaquette stabilizers for the $[[15, 1, 3]]$ qRM code. Only ten of them are independent due to the constraints of Table VI. In the simulations, we decided to measure the set of ten independent stabilizers $\{p_1, p_2, p_3, p_7, p_8, p_9, p_{13}, p_{16}, p_{17}, p_{18}\}$.

qRM: X -type stabilizers	
c_1	$X_1 X_2 X_6 X_7 X_8 X_9 X_{13} X_{14}$
c_2	$X_4 X_5 X_6 X_7 X_{11} X_{12} X_{13} X_{14}$
c_3	$X_2 X_3 X_4 X_7 X_9 X_{10} X_{11} X_{14}$
c_4	$X_8 X_9 X_{10} X_{11} X_{12} X_{13} X_{14} X_{15}$

TABLE V. X -type 3-cell stabilizers for the $[[15, 1, 3]]$ qRM code.

qRM: Independent constraints			
Γ_1	$p_4 p_5 p_{10} p_{11}$	Γ_5	$p_6 p_7 p_{11} p_{12}$
Γ_2	$p_1 p_5 p_{10} p_{16}$	Γ_6	$p_2 p_6 p_{12} p_{17}$
Γ_3	$p_8 p_9 p_{10} p_{12}$	Γ_7	$p_{13} p_{15} p_{16} p_{17}$
Γ_4	$p_3 p_8 p_{10} p_{18}$	Γ_8	$p_{14} p_{15} p_{16} p_{18}$

TABLE VI. Independent set of constraints $\Gamma_i = I$ (identity) with $i = 1, 2, \dots, 8$ for the $[[15, 1, 3]]$ qRM code.

The minimum weight logical- Z operator \bar{Z} has weight-3, and a representative lies at the edge of the tetrahedron

$$\bar{Z} = Z_1 Z_2 Z_3. \quad (3)$$

The minimum weight logical- X operator \bar{X} has weight-7, and a representative lies at the face of a boundary of the tetrahedron

$$\bar{X} = X_1 X_2 X_3 X_4 X_5 X_6 X_7. \quad (4)$$

Hence, the distance $d = \min\{d_x, d_z\} = 3$, where $d_x = 7$ is the distance for X -type logical operators, and $d_z = 3$ is the distance for Z -type logical operators. In addition, the $[[15, 1, 3]]$ qRM code is capable of correcting arbitrary weight-1 Z -errors (phase-flip) and up to weight-3 X -errors (bit-flip).

The qRM code also admits a transversal T -gate \bar{T} , consisting of single-qubit T/T^\dagger gates applied to odd/even labeled qubits, respectively,

$$\bar{T} = T_1 T_2^\dagger T_3 T_4^\dagger T_5 T_6^\dagger T_7 T_8^\dagger T_9 T_{10}^\dagger T_{11} T_{12}^\dagger T_{13} T_{14}^\dagger T_{15}, \quad (5)$$

where the single qubit T -gate is defined as

$$T_j = \begin{pmatrix} 1 & 0 \\ 0 & e^{i\frac{\pi}{4}} \end{pmatrix}. \quad (6)$$

Note that since the S -gate $\bar{S} = \bar{T}^2$, the qRM code trivially supports a transversal logical \bar{S} gate in terms of single qubit S/S^\dagger -gates, respectively,

$$\bar{S} = S_1 S_2^\dagger S_3 S_4^\dagger S_5 S_6^\dagger S_7 S_8^\dagger S_9 S_{10}^\dagger S_{11} S_{12}^\dagger S_{13} S_{14}^\dagger S_{15}. \quad (7)$$

Even though the $[[15, 1, 3]]$ qRM supports a transversal non-Clifford gate, it does not support a transversal Haddamard gate \bar{H} , as this would violate Eastin-Knill theorem [51].

IV. PROTOCOL

Our protocol aims to prepare a magic state encoded in the Steane code. At the logical level, our approach uses the standard one-bit teleportation protocol [52] to teleport the magic state $|\bar{T}\rangle$ encoded in the qRM code to the Steane code, see Fig. 3.

We now describe each of the components in Fig. 3. How to apply each component fault-tolerantly has been well-known in the literature [20, 21, 35, 36]. Our main contribution is a novel protocol for the preparation of the $|\bar{+}\rangle$ of the qRM code and the $\overline{\text{CNOT}}$ gate, which yields an overall improvement compared to the known methods.

For completeness, we first describe the standard methods we employ. For the logical \bar{T} gate of the qRM code, we apply the standard transversal gate (5) [4, 35]. For the logical- X measurement necessary for the teleportation, we first measure all the qubits of the qRM code in the X -basis. Then, we compute the X -syndrome (see Tab. V) in post-processing. At

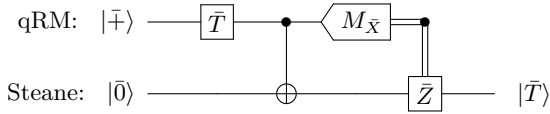


FIG. 3. Protocol at the logical level. A qRM (quantum Reed-Muller) and the Steane codeblock are prepared in the $|+\rangle$ and the $|0\rangle$ state, respectively. The transversal logical T gate native to the qRM code is applied, creating a logical magic state $|\bar{T}\rangle = T|+\rangle$. The magic state is then teleported to the Steane codeblock by applying a logical CNOT gate, measuring the logical \bar{X} operator and applying a logical \bar{Z} correction in case that $\bar{X} = -1$. At the end of the protocol, the logical magic state $|\bar{T}\rangle$ is prepared in the Steane codeblock.

this point, we have a choice to either apply error correction, or instead post-select on measuring a trivial syndrome. We opt for the latter, since that yields a lower logical infidelity. After post-selecting for a trivial X -syndrome, we extract the value of the logical- X operator \bar{X} , and we apply a logical- Z correction on the Steane code in case that $\bar{X} = -1$. The $|0\rangle$ state preparation of the Steane code follows the known protocol of Ref. [49, 53]; see Fig. 4. The logical- Z correction on the Steane code uses the standard weight-3 logical operator (1).

Lastly, since the final magic state is encoded in the Steane code, an additional round of flagged-based error correction could be used to detect further errors as in Ref. [20, 49], at the expense of increasing the overhead cost of the protocol. Given the depth of syndrome extraction circuits of Sec. IV A, we decided not to incorporate this variation.

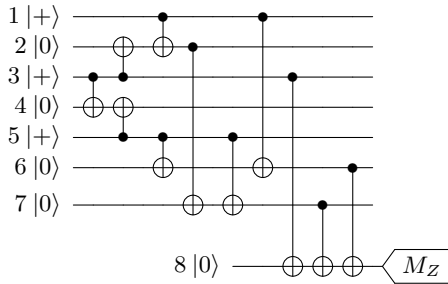


FIG. 4. Preparation of the logical zero state $|0\rangle$ in the Steane code. A non-fault tolerant initialization involves preparing the physical qubits either in the zero $|0\rangle$ or plus $|+\rangle$ state, followed by a series of CNOT gates. A final verification step measures the logical \bar{Z} operator and uses an ancilla qubit acting as flag, detecting all weight-2 X -errors originating from a single X -error.

A. Preparation of $|+\rangle$ for qRM code

The most involved part of our protocol is the preparation of the $|+\rangle$ for the qRM code. At a high level, our approach prepares the logical $|+\rangle$ state using the method in Ref. [23], followed by a flag-based error detection [19–21, 54]. Our flag-based error detection scheme employs the scheme of Ref. [20], which is appropriated to the qRM code.

The first step of this protocol is described in Fig. 5. The final verification step measures the logical \bar{X} operator and uses an ancilla qubit acting as flag, detecting all uncorrectable weight-2 Z -errors originating from a single Z -error.

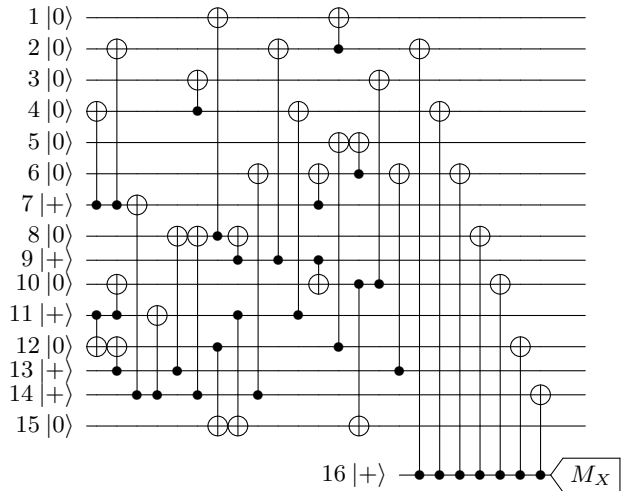


FIG. 5. Preparation of the logical plus state $|+\rangle$ in the qRM code. A non-fault tolerant initialization involves preparing the physical qubits either in the zero $|0\rangle$ or plus $|+\rangle$ state, followed by a series of CNOT gates.

At this point, the state prepared may have additional X -errors. If we do not correct them, they will propagate through the transversal T -gate to a XS -error, which will lead to an error in the final measurement $M_{\bar{X}}$ of the qRM code. In order to mitigate this effect, one must measure the Z -type syndromes. Such measurements should be chosen carefully. If we were to measure each Z -type syndrome using the standard approach (i.e., using a single ancilla and 4 CNOTs), a single fault can propagate to weight-2 errors in the data block.

We can avoid this problem by using the flag-based syndrome-extraction circuit for the Steane code [20]. In that paper, the authors introduced two types of syndrome extraction circuits, one extracting two syndromes at once and the other extracting three syndromes at once; see Fig. 6 and Fig. 7. There are 10 independent Z -type stabiliz-

ers, see Table IV, which we can organize as follows. First, we can measure $(Z_8Z_{12}Z_{13}Z_{15}, Z_5Z_6Z_{12}Z_{13})$ and $(Z_3Z_4Z_{10}Z_{11}, Z_4Z_5Z_{11}Z_{15})$ using Fig. 6. Then we can measure $(Z_1Z_2Z_6Z_7, Z_2Z_3Z_4Z_7, Z_4Z_5Z_6Z_7)$ and $(Z_8Z_9Z_{13}Z_{14}, Z_9Z_{10}Z_{11}Z_{14}, Z_{11}Z_{12}Z_{13}Z_{14})$ using Fig. 7. Flags and syndromes are postselected to be +1. We remark that there are other set of stabilizers one may choose to measure. We leave such studies for future work.

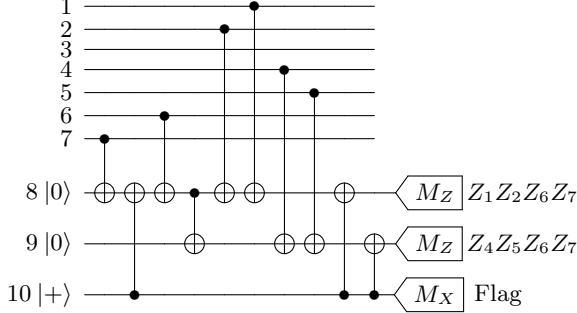


FIG. 6. Simultaneous flagged syndrome extraction circuit for two Z -type stabilizers in the Steane code. An additional qubit prepared in the plus state $|+\rangle$ acts as a flag and detects higher weight data Z -errors originating from arbitrary single qubit ancilla Z -errors.

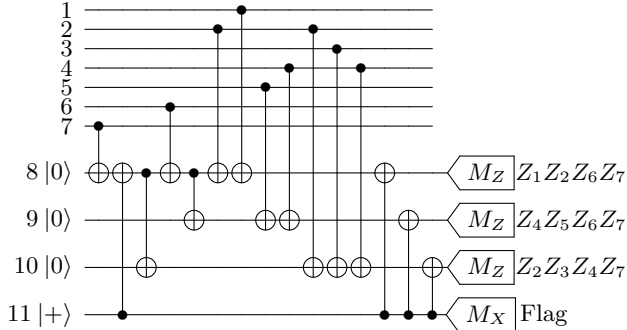


FIG. 7. Simultaneous flagged syndrome extraction circuit for three Z -type stabilizers in the Steane code. An additional qubit prepared in the plus state $|+\rangle$ acts as a flag and detects higher weight data Z -errors originating from arbitrary single qubit ancilla Z -errors.

B. Transversal CNOT gate

The logical $\overline{\text{CNOT}}$ gate in Fig. 3 can be implemented using a transversal gate. With respect to the convention described in Fig. 1 and 2, we can

apply the following operation:

$$\overline{\text{CNOT}} = \bigotimes_{i=1}^7 \text{CNOT}_i, \quad (8)$$

where CNOT_i is the CNOT gate whose control and target is the i 'th qubit of the qRM and Steane code, respectively.

This gate preserves the stabilizer group and satisfies the following relations:

$$\begin{aligned} \overline{\text{CNOT}} \bar{X}_{\text{qRM}} \overline{\text{CNOT}} &= \bar{X}_{\text{qRM}} \bar{X}_{\text{S}} \\ \overline{\text{CNOT}} \bar{Z}_{\text{S}} \overline{\text{CNOT}} &= \bar{Z}_{\text{qRM}} \bar{Z}_{\text{S}} \end{aligned} \quad (9)$$

up to stabilizers, where \bar{X}_{qRM} and \bar{Z}_{qRM} are logical X - and Z -operators of the qRM code, (4) and (3); similarly \bar{X}_{S} and \bar{Z}_{S} are logical X - and Z -operators of the Steane code, (2) and (1). Thus Eq. (8) is a logical CNOT from the qRM code to the Steane code. A generalization of this construction to the entire 3D and 2D color code family is discussed in Ref. [39].

V. SIMULATION

The protocol described in Section IV uses 22 data qubits and 16 ancilla qubits. If the ancilla qubits are reused, it is possible to reduce the ancilla qubit requirements to 4, which is bottlenecked by the flag circuit in Fig. 7. Even so, an exact *mixed state* simulation of 26 qubits is challenging.

As such, we resort to a Monte Carlo sampling-based approach. We keep track of the Pauli errors, which after passing through \bar{T} , become Clifford errors. Thus by studying an *ensemble* of circuits, each suffering from a random Clifford error, we can simulate the performance of our protocol. This is a novel simulation technique akin to an extended stabilizer simulator, which effectively incorporates the non-Clifford T -gate.

To incorporate the stochastic Clifford errors into the simulation, we first initialize the noisy logical plus state $|\bar{+}\rangle$ in the qRM code as in Fig. 3 and extract the Pauli error frame P ,

$$|\bar{+}\rangle = P|\bar{+}\rangle_{\text{noiseless}}, \quad (10)$$

where $|\bar{+}\rangle_{\text{noiseless}}$ is the noiseless plus state. Since the T -gate has to be applied to the noisy plus state,

$$\bar{T}|\bar{+}\rangle = (\bar{T}P\bar{T}^\dagger)\bar{T}|\bar{+}\rangle_{\text{noiseless}} = C(P)|\bar{T}\rangle_{\text{noiseless}}. \quad (11)$$

The state $|\bar{T}\rangle_{\text{noiseless}} = \bar{T}|\bar{+}\rangle_{\text{noiseless}}$ is a noiseless magic state in the qRM code and $C(P) = \bar{T}P\bar{T}^\dagger$ is

the Clifford error frame. If $P \sim \bigotimes_{i=1}^{15} X^{a_i} Z^{b_i}$ for $a_i, b_i \in \{0, 1\}$, then the Clifford error frame becomes

$$C(P) \sim \left(\bigotimes_{i \text{ odd}} S^{a_i} \right) \left(\bigotimes_{i \text{ even}} S^{\dagger a_i} \right) P, \quad (12)$$

up to a global phase. We remark that there is an important subtlety in this simulation, which if remain not accounted for, could report a higher logical error rate than the the correct one. The Pauli error frame P (10) is equivalent to another frame up to stabilizers and a logical- X operator (ignoring the global phase). To illustrate this point, suppose that the error is equivalent to a stabilizer, which should not affect the state. However, if that stabilizer is conjugated by \bar{T} , it results in a product of phase gates that can influence the simulation at the future steps causing a logical failure. In order to avoid this computational issue, once extracted P , we replaced it by the equivalent minimum weight Pauli error frame up to stabilizers and a logical- X operator. This effect is not negligible; we have observed a factor of few difference in the logical error rate, depending on whether we correct this issue or not.

After updating the Pauli errors to Clifford errors, we effectively have an ensemble of encoded $|\bar{T}\rangle_{\text{noiseless}}$ states of the qRM code followed by a stochastic Clifford noise. Note that for a magic state $|\bar{T}\rangle$, the density matrix $|\bar{T}\rangle\langle\bar{T}|$ can be written as a linear combination of pure stabilizer states:

$$\begin{aligned} |\bar{T}\rangle\langle\bar{T}| &= I + \frac{\sqrt{2}}{4} (|\bar{+}\rangle\langle\bar{+}| - |\bar{-}\rangle\langle\bar{-}|) \\ &+ \frac{\sqrt{2}}{4} (|\bar{Y}_+\rangle\langle\bar{Y}_+| - |\bar{Y}_-\rangle\langle\bar{Y}_-|). \end{aligned} \quad (13)$$

All these states can be implemented by applying logical transversal gates to the logical plus state in the qRM code: $|\bar{-}\rangle = \bar{Z}|\bar{+}\rangle$, $|\bar{Y}_+\rangle = \bar{S}|\bar{+}\rangle$ and $|\bar{Y}_-\rangle = \bar{S}^\dagger|\bar{+}\rangle$. For each of the stabilizer states appearing in Eq. (13), we can estimate the fidelity between the logical noiseless state in the Steane code $|\bar{T}\rangle_{\text{Steane}}$ (after teleportation) and the given noisy final state $\bar{\rho}$ using the following relation:

$$\langle\bar{T}|\bar{\rho}|\bar{T}\rangle_{\text{Steane}} = \frac{1}{2} + \frac{\sqrt{2}}{4} (\langle\bar{X}\rangle_{\bar{\rho}} + \langle\bar{Y}\rangle_{\bar{\rho}}), \quad (14)$$

where $\langle\bar{X}\rangle_{\bar{\rho}}$ and $\langle\bar{Y}\rangle_{\bar{\rho}}$ are the expectation values of the logical X and Y operators evaluated with respect to the code state $\bar{\rho}$.

In our simulation, the state $\bar{\rho}$ is chosen to be the (normalized) post-selected state that we obtain at the very end of the protocol. Because the post-selection probability is identical for every stabilizer state appearing in Eq. (13), we can estimate Eq. (14) by taking the expectation value of the logical X and

Y operator of the Steane code only for the post-selected events. Indeed, by combining (13) and (14) the fidelity can be conveniently written as

$$\langle\bar{T}|\bar{\rho}|\bar{T}\rangle_{\text{Steane}} = \frac{1}{2} + \frac{1}{8}\Delta, \quad (15)$$

where

$$\begin{aligned} \Delta &= \left(\langle\bar{X}\rangle_{|\bar{+}\rangle} - \langle\bar{X}\rangle_{|\bar{-}\rangle} + \langle\bar{X}\rangle_{|\bar{Y}_+\rangle} - \langle\bar{X}\rangle_{|\bar{Y}_-\rangle} \right) \\ &+ \left(\langle\bar{Y}\rangle_{|\bar{+}\rangle} - \langle\bar{Y}\rangle_{|\bar{-}\rangle} + \langle\bar{Y}\rangle_{|\bar{Y}_+\rangle} - \langle\bar{Y}\rangle_{|\bar{Y}_-\rangle} \right). \end{aligned} \quad (16)$$

We quantify the quality of magic state using two different methods. In the first approach, we compute the fidelity using Eq. (15) and (16) assuming that at the final step we perform logical measurement. That is, we measure all the qubits in the X -, or Y - basis and obtain the syndrome information from the measurement outcomes (recall that in the Steane code, since the stabilizer generators have weight-4, it is possible to get the Z -syndrome by multiplying the X and Y -syndromes, respectively). From the syndrome information, a correction is deduced, after which we obtain the logical measurement outcome. This approach roughly quantifies the quality of the magic state encoded in the Steane code.

In the second approach, in the last step we post-select on measuring a trivial syndrome. This can be used as a proxy for the lowest error rate one can achieve if one were to later enlarge the code to a larger one whilst post-selecting [24, 25]. However, as pointed out in Ref. [25], the logical error rate obtained after such enlargement process is often higher than the one obtained prior to that stage. How the logical error rate changes under such a process is beyond the scope of this paper, and we leave it for a future work.

A. Noise model

We use the standard noise model in which every operation is followed or preceded by a noisy process; we use the uniform depolarizing noise model of strength p . For state preparation, we assume that there is a probability p of flipping the initial state. Hence, we model the preparation of a $|0\rangle$ state as perfect $|0\rangle$ followed by a bit flip X applied with probability p . Similarly, the preparation of a $|+\rangle$ state is modeled as a perfect $|+\rangle$ state followed by a phase flip Z with probability p .

For measurements, we follow a similar recipe as for state preparation. We model a Z -type measurement as a bit flip X applied with probability p , followed by a perfect Z -type measurement. Similarly,

we model a X -type measurement as a phase flip Z applied with probability p , followed by a perfect X -type measurement.

For single and two qubit gates, we model them as perfect gates followed by the depolarizing error model. For 1-qubit gates, the depolarizing error model leaves the state unaltered with probability $1 - p$, and applies a Pauli error $P \in \{X, Y, Z\}$ (denoted as \mathcal{P}_1) with probability $\frac{p}{3}$. For 2-qubit gates, the depolarizing error model leaves the state unaltered with probability $1 - p$, and applies a Pauli error $P \otimes Q$ with $P, Q \in \{I, X, Y, Z\}$ (denoted as \mathcal{P}_2) and $P \otimes Q \neq I \otimes I$ with probability $\frac{p}{15}$. Specifically, these channels can be written as follows

$$\mathcal{D}_1(\rho) = (1 - p)\rho + \sum_{P \in \mathcal{P}_1/\{I\}} \frac{p}{3} P\rho P, \quad (17)$$

$$\mathcal{D}_2(\rho) = (1 - p)\rho + \sum_{P \in \mathcal{P}_2/\{I \otimes I\}} \frac{p}{15} P\rho P. \quad (18)$$

Here, \mathcal{D}_1 and \mathcal{D}_2 are a single- and two-qubit depolarizing noise model, respectively.

Regarding idling errors, we did not consider them in our simulations. Given the depths of the different circuits present in our protocol, their contribution may not be completely negligible for experimental purposes.

In order to compare our findings with other state-of-the-art results in the literature, some simulations were done with the multiparameter depolarizing error model too, see Table II. This model is defined similarly as the uniform counterpart, with the only difference that each type of error can be tuned independently, and they are parameterized by: p_i initialization error, p_m measurement error, p_1 and p_2 single- and two-qubit error gate.

B. Simulation Methods

Our simulations were done using the stabilizer simulator package Stim [55] for Python. Specifically, using Pauli frames obtained from the functions `FlipSimulator()` and `peek_pauli_flips()`, we generated random instances of Clifford errors, each of which were later incorporated to the full circuit using again Stim. For a given simulation, we ran N_{tot} Monte Carlo shots, and postselected N_{post} of them. Hence, the acceptance rate of the protocol is given by

$$p_{\text{accept}} = \frac{N_{\text{post}}}{N_{\text{tot}}}. \quad (19)$$

For later reference, the post-selection rejection probabilities are defined as the complement of the accep-

tance rate (19), in other words

$$p_{\text{reject}} = 1 - p_{\text{accept}}. \quad (20)$$

Similarly, the infidelity of the magic state quantifies the logical failure and is defined as the complement of the infidelity (15) and (16),

$$p_{\text{fail}} = 1 - \langle \bar{T} | \bar{\rho} | \bar{T} \rangle_{\text{Steane}}. \quad (21)$$

The total number of shots N_{tot} ranged from 10^7 up to 3×10^8 . This is because when computing the expectation values $\langle \bar{P} \rangle_{\bar{\rho}}$ for $P = X, Y$, the uncertainty is given by

$$\sigma_{P, \bar{\rho}} = \sqrt{\frac{\text{Var}(\langle \bar{P} \rangle_{\bar{\rho}})}{N_{\text{post}}}}. \quad (22)$$

We observed that at low error rates, the major contribution to the variance came from the intrinsic probabilistic nature of the measurement of an eigenstate of a Pauli P in another basis P' . More precisely, when computing in (15) and (16) the expected values $\langle \bar{X} \rangle_{|\bar{Y}_{\pm}\rangle}$ and $\langle \bar{Y} \rangle_{|\bar{X}_{\pm}\rangle}$. In a noiseless scenario, we can model the measurement outcomes as a Bernoulli distribution that returns $+1$ and -1 with even probability $1/2$, which has variance 1. Thus, yielding an error of $\sigma_{P, \bar{\rho}} \gtrsim 1/\sqrt{N_{\text{post}}}$ for the aforementioned four expected values. Finally, taking into account normalization factors in (15) and (16), this implies that the propagated fidelity error is roughly given by $\sigma_{\langle \bar{T} | \bar{\rho} | \bar{T} \rangle_{\text{Steane}}} \gtrsim 1/(4\sqrt{N_{\text{post}}})$.

C. Results

As we stated before in Section V, we consider two approaches. The first approach performs error correction when measuring the logical X and Y used in Eq. (15) and (16). The second approach uses post-selection on measuring trivial syndrome at this step.

The results of the simulation for both approaches are plotted in Fig. 8 and 9. In the first and the second approach, our circuit can detect all faults of weight 1 and 2, respectively; this difference comes from the final logical measurement stage. We have fitted the logical infidelity and the post-selection probability to a polynomial. From the fitted polynomial for the infidelity we obtained at leading order,

$$p_{\text{fail}} \approx \begin{cases} 25.5p^2 - 1266.7p^3 + 165884.4p^4 + \dots & \text{(error correction),} \\ 508.5p^3 + 4477.1p^4 & \text{(post-selection).} \end{cases} \quad (23)$$

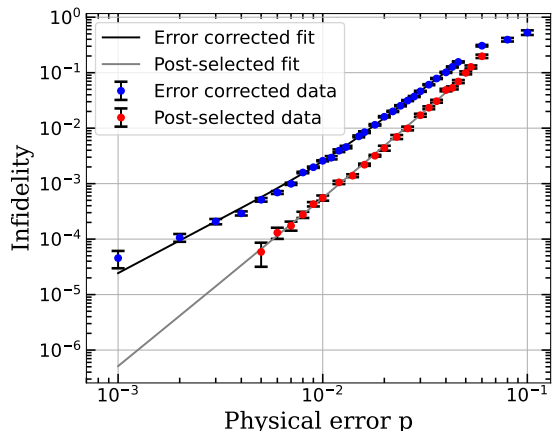


FIG. 8. Infidelity of magic states $|\bar{T}\rangle$ as a function of physical error rate for a uniform depolarizing error model of strength p . The polynomial fits with their respective parameters are explicitly given in Eq. (23).

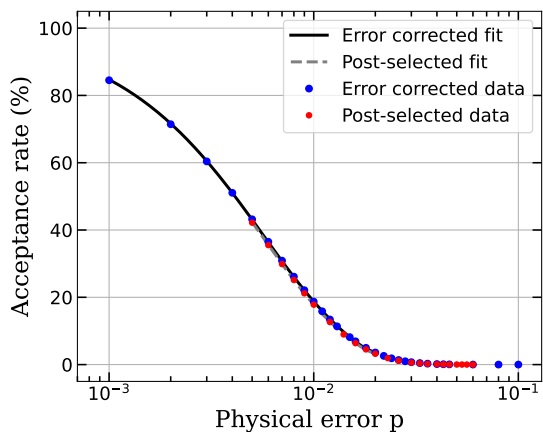


FIG. 9. Acceptance rate of magic states $|\bar{T}\rangle$ as a function of physical error rate for a uniform depolarizing error model of strength p . The polynomial fits with their respective parameters are explicitly given in Eq. (24). For physical error rates $p \leq 10^{-2}$, the difference between both data sets is smaller than 1%.

In addition, at leading order the polynomial fits for the rejection rates yield,

$$p_{\text{reject}} \approx \begin{cases} 164.6p - 12362.8p^2 + 477206.9p^3 + \dots & \text{(error correction),} \\ 166.4p - 12352.7p^2 + 462706.3p^3 + \dots & \text{(post-selection).} \end{cases} \quad (24)$$

It is worth pointing out that for $p \in [10^{-3}, 10^{-2}]$ the leading and sub-leading terms of the polynomial

fits (23) have the same order of magnitude. Hence, even though the polynomial interpolates the data points in that regime, caution need to be taken in case of extrapolation for even lower probabilities $p \ll 10^{-3}$. A similar note should we addressed in relation our reported result of 5.1×10^{-7} in Table I for the infidelity of the post-selected state when $p = 10^{-3}$. Notwithstanding, the extrapolation was done from a nearby error rate $p = 5 \times 10^{-3}$, and roughly twenty data points with different error rates were simulated in order to account for a robust fitting polynomial.

VI. DISCUSSION

In this paper, we introduced a new method for preparing a high-fidelity magic state using color codes. Our approach employs a judicious use of flag-based post-selection and a novel transversal gate (that is equivalent up to a transversal unitary to the recently discovered gate in Ref. [39], which appeared during the preparation of this manuscript). An important question at this point is whether one can achieve an even higher fidelity magic state by using a similar protocol, with a flag-based post-selection approach on a larger 3D color code. There are several problems that need to be solved for such a study. First of all, we need to generalize our syndrome extraction circuit to the larger instances of the 3D code. Secondly, a better simulation method must be developed. The infidelity of the magic state produced this way is expected to be multiple orders of magnitude lower than what is reported in this manuscript. Simulation of such low error rate will be extremely challenging using a Monte Carlo approach. (For instance, Ref. [25] reported weeks of performing a Monte Carlo simulation and it is not even clear if that will be enough for this study.) And a naive density matrix simulation of the full circuit is likely out of reach for classical computers. Perhaps a tensor network calculation can be useful for this purpose. We leave these studies for future work.

Another important future research direction is an end-to-end analysis of the fidelity of the magic state. In order to use our high-fidelity magic state, one must convert the given state on the original 2D color code to a larger 2D lattice, employing post-selection in this process. It was found in a recent study that there is a non-negligible difference between the logical error rate obtained before and after this process [25]. The ratio between the two should depend on the details about the effective error model induced on the 2D color code patch which is influenced by the protocol. As such, it is not completely clear if the ratio reported in Ref. [25] would remain the same if their growing process is applied to our setup.

Understanding this would require a yet another challenging large-scale simulation.

Lastly, we note that our approach should be readily implementable in platforms that allow all-to-all connectivities such as the ion trap [56, 57] and neutral atom-based quantum computers [48]. Optimizing our protocol for these platforms and experimentally demonstrating a substantial improvement in the magic state infidelity will be an important experimental outcome that we anticipate to be achievable in the near term.

ACKNOWLEDGEMENTS

LD was supported by funds from the University of California, Davis and by the Dean’s Summer Graduate Support Award 2024 from the College of Letters and Science of the University of California, Davis. IK acknowledges support from NSF under award number QCIS-FF-2013562. We thank Craig Gidney for helpful discussions and Sascha Heußen for providing comments on the final manuscript.

-
- [1] P. W. Shor, Scheme for reducing decoherence in quantum computer memory, *Phys. Rev. A* **52**, R2493 (1995).
- [2] D. Aharonov and M. Ben-Or, Fault-tolerant quantum computation with constant error, in *Proceedings of the twenty-ninth annual ACM symposium on Theory of computing* (1997) pp. 176–188.
- [3] D. Gottesman, Fault-tolerant quantum computation with constant overhead, arXiv preprint arXiv:1310.2984 (2013).
- [4] S. Bravyi and A. Kitaev, Universal quantum computation with ideal clifford gates and noisy ancillas, *Physical Review A—Atomic, Molecular, and Optical Physics* **71**, 022316 (2005).
- [5] A. M. Meier, B. Eastin, and E. Knill, Magic-state distillation with the four-qubit code, arXiv preprint arXiv:1204.4221 (2012).
- [6] S. Bravyi and J. Haah, Magic-state distillation with low overhead, *Physical Review A—Atomic, Molecular, and Optical Physics* **86**, 052329 (2012).
- [7] C. Jones, Low-overhead constructions for the fault-tolerant toffoli gate, *Physical Review A* **87**, 022328 (2013).
- [8] A. G. Fowler, S. J. Devitt, and C. Jones, Surface code implementation of block code state distillation, *Scientific reports* **3**, 1939 (2013).
- [9] C. Jones, Multilevel distillation of magic states for quantum computing, *Physical Review A—Atomic, Molecular, and Optical Physics* **87**, 042305 (2013).
- [10] G. Duclos-Cianci and K. M. Svore, Distillation of nonstabilizer states for universal quantum computation, *Physical Review A—Atomic, Molecular, and Optical Physics* **88**, 042325 (2013).
- [11] G. Duclos-Cianci and D. Poulin, Reducing the quantum-computing overhead with complex gate distillation, *Physical Review A* **91**, 042315 (2015).
- [12] E. T. Campbell and M. Howard, Unified framework for magic state distillation and multiqubit gate synthesis with reduced resource cost, *Physical Review A* **95**, 022316 (2017).
- [13] J. O’Gorman and E. T. Campbell, Quantum computation with realistic magic-state factories, *Physical Review A* **95**, 032338 (2017).
- [14] J. Haah and M. B. Hastings, Codes and protocols for distilling t , controlled- s , and toffoli gates, *Quantum* **2**, 71 (2018).
- [15] C. Gidney and A. G. Fowler, Efficient magic state factories with a catalyzed $|CCZ\rangle$ to $2|T\rangle$ transformation, *Quantum* **3**, 135 (2019).
- [16] A. G. Fowler and S. J. Devitt, [A bridge to lower overhead quantum computation](#) (2013), arXiv:1209.0510 [quant-ph].
- [17] D. Litinski, Magic State Distillation: Not as Costly as You Think, *Quantum* **3**, 205 (2019).
- [18] Y. Li, A magic state’s fidelity can be superior to the operations that created it, *New Journal of Physics* **17**, 023037 (2015).
- [19] T. J. Yoder and I. H. Kim, The surface code with a twist, *Quantum* **1**, 2 (2017).
- [20] R. Chao and B. W. Reichardt, Quantum error correction with only two extra qubits, *Physical review letters* **121**, 050502 (2018).
- [21] R. Chao and B. W. Reichardt, Fault-tolerant quantum computation with few qubits, *npj Quantum Information* **4**, 42 (2018).
- [22] C. Chamberland and K. Noh, Very low overhead fault-tolerant magic state preparation using redundant ancilla encoding and flag qubits, *npj Quantum Information* **6**, 91 (2020).
- [23] F. Butt, S. Heußen, M. Rispler, and M. Müller, Fault-tolerant code-switching protocols for near-term quantum processors, *PRX Quantum* **5**, 020345 (2024).
- [24] T. Itogawa, Y. Takada, Y. Hirano, and K. Fujii, Even more efficient magic state distillation by zero-level distillation, arXiv preprint arXiv:2403.03991 (2024).
- [25] C. Gidney, N. Shutty, and C. Jones, [Magic state cultivation: growing \$t\$ states as cheap as cnot gates](#) (2024), arXiv:2409.17595 [quant-ph].
- [26] I. Pogorelov, F. Butt, L. Postler, C. D. Marciniak, P. Schindler, M. Müller, and T. Monz, Experimental fault-tolerant code switching, arXiv preprint arXiv:2403.13732 (2024).
- [27] S.-H. Lee, F. Thomsen, N. Fazio, B. J. Brown, and S. D. Bartlett, [Low-overhead magic state distillation with color codes](#) (2024), arXiv:2409.07707 [quant-ph].
- [28] E. T. Campbell, Early fault-tolerant simulations of the hubbard model, *Quantum Science and Technol-*

- ogy **7**, 015007 (2021).
- [29] J. Lee, D. W. Berry, C. Gidney, W. J. Huggins, J. R. McClean, N. Wiebe, and R. Babbush, Even more efficient quantum computations of chemistry through tensor hypercontraction, *PRX Quantum* **2**, 030305 (2021).
- [30] V. von Burg, G. H. Low, T. Häner, D. S. Steiger, M. Reiher, M. Roetteler, and M. Troyer, Quantum computing enhanced computational catalysis, *Physical Review Research* **3**, 033055 (2021).
- [31] C. Gidney, Halving the cost of quantum addition, *Quantum* **2**, 74 (2018).
- [32] I. H. Kim, Y.-H. Liu, S. Pallister, W. Pol, S. Roberts, and E. Lee, Fault-tolerant resource estimate for quantum chemical simulations: Case study on li-ion battery electrolyte molecules, *Physical Review Research* **4**, 023019 (2022).
- [33] A. Delgado, P. A. M. Casares, R. dos Reis, M. S. Zini, R. Campos, N. Cruz-Hernández, A.-C. Voigt, A. Lowe, S. Jahangiri, M. A. Martin-Delgado, J. E. Mueller, and J. M. Arrazola, Simulating key properties of lithium-ion batteries with a fault-tolerant quantum computer, *Phys. Rev. A* **106**, 032428 (2022).
- [34] Y. Su, D. W. Berry, N. Wiebe, N. Rubin, and R. Babbush, Fault-tolerant quantum simulations of chemistry in first quantization, *PRX Quantum* **2**, 040332 (2021).
- [35] H. Bombin and M. A. Martin-Delgado, Topological computation without braiding, *Phys. Rev. Lett.* **98**, 160502 (2007).
- [36] H. Bombin and M. A. Martin-Delgado, Topological quantum distillation, *Phys. Rev. Lett.* **97**, 180501 (2006).
- [37] H. Bombín, Dimensional jump in quantum error correction, *New Journal of Physics* **18**, 043038 (2016).
- [38] M. E. Beverland, A. Kubica, and K. M. Svore, Cost of universality: A comparative study of the overhead of state distillation and code switching with color codes, *PRX Quantum* **2**, 020341 (2021).
- [39] S. Heußen and J. Hilder, [Efficient fault-tolerant code switching via one-way transversal cnot gates](#) (2024), [arXiv:2409.13465 \[quant-ph\]](#).
- [40] M. Kjaergaard, M. E. Schwartz, J. Braumüller, P. Krantz, J. I.-J. Wang, S. Gustavsson, and W. D. Oliver, Superconducting qubits: Current state of play, *Annual Review of Condensed Matter Physics* **11**, 369 (2020).
- [41] E. Knill, R. Laflamme, and G. J. Milburn, A scheme for efficient quantum computation with linear optics, *nature* **409**, 46 (2001).
- [42] S. Bartolucci, P. Birchall, H. Bombin, H. Cable, C. Dawson, M. Gimeno-Segovia, E. Johnston, K. Kieling, N. Nickerson, M. Pant, *et al.*, Fusion-based quantum computation, *Nature Communications* **14**, 912 (2023).
- [43] J. E. Bourassa, R. N. Alexander, M. Vasmer, A. Patil, I. Tzitrin, T. Matsuura, D. Su, B. Q. Baragiola, S. Guha, G. Dauphinais, K. K. Sabapathy, N. C. Menicucci, and I. Dhand, Blueprint for a Scalable Photonic Fault-Tolerant Quantum Computer, *Quantum* **5**, 392 (2021).
- [44] J. I. Cirac and P. Zoller, Quantum computations with cold trapped ions, *Phys. Rev. Lett.* **74**, 4091 (1995).
- [45] C. Monroe and J. Kim, Scaling the ion trap quantum processor, *Science* **339**, 1164 (2013).
- [46] C. D. Bruzewicz, J. Chiaverini, R. McConnell, and J. M. Sage, Trapped-ion quantum computing: Progress and challenges, *Applied Physics Reviews* **6** (2019).
- [47] D. Bluvstein, H. Levine, G. Semeghini, T. T. Wang, S. Ebadi, M. Kalinowski, A. Keesling, N. Maskara, H. Pichler, M. Greiner, *et al.*, A quantum processor based on coherent transport of entangled atom arrays, *Nature* **604**, 451 (2022).
- [48] D. Bluvstein, S. J. Evered, A. A. Geim, S. H. Li, H. Zhou, T. Manovitz, S. Ebadi, M. Cain, M. Kalinowski, D. Hangleiter, *et al.*, Logical quantum processor based on reconfigurable atom arrays, *Nature* **626**, 58 (2024).
- [49] L. Postler, S. Heußen, I. Pogorelov, M. Rispler, T. Feldker, M. Meth, C. D. Marciniak, R. Stricker, M. Ringbauer, R. Blatt, *et al.*, Demonstration of fault-tolerant universal quantum gate operations, *Nature* **605**, 675 (2022).
- [50] A. Steane, Multiple-particle interference and quantum error correction, *Proceedings of the Royal Society of London. Series A: Mathematical, Physical and Engineering Sciences* **452**, 2551 (1996).
- [51] B. Eastin and E. Knill, Restrictions on transversal encoded quantum gate sets, *Physical review letters* **102**, 110502 (2009).
- [52] X. Zhou, D. W. Leung, and I. L. Chuang, Methodology for quantum logic gate construction, *Physical Review A* **62**, 052316 (2000).
- [53] H. Goto, Minimizing resource overheads for fault-tolerant preparation of encoded states of the steane code, *Scientific reports* **6**, 19578 (2016).
- [54] B. W. Reichardt, Fault-tolerant quantum error correction for steane's seven-qubit color code with few or no extra qubits, *Quantum Science and Technology* **6**, 015007 (2020).
- [55] C. Gidney, Stim: a fast stabilizer circuit simulator, *Quantum* **5**, 497 (2021).
- [56] M. DeCross, R. Haghshenas, M. Liu, Y. Alexeev, C. H. Baldwin, J. P. Bartolotta, M. Bohn, E. Chertkov, J. Colina, D. DelVento, *et al.*, The computational power of random quantum circuits in arbitrary geometries, *arXiv preprint arXiv:2406.02501* (2024).
- [57] C. Löschnauer, J. M. Toba, A. Hughes, S. King, M. Weber, R. Srinivas, R. Matt, R. Nourshargh, D. Allcock, C. Ballance, *et al.*, Scalable, high-fidelity all-electronic control of trapped-ion qubits, *arXiv preprint arXiv:2407.07694* (2024).